

THORIUM BASED MIRRORS FOR HIGH REFLECTIVITY  
IN THE EUV

by

Jedediah Edward Jensen Johnson

Submitted to the Department of Physics and Astronomy in partial fulfillment  
of graduation requirements for the degree of  
Bachelor of Science

Brigham Young University

August 2004

Advisor: David D. Allred

Honors Representative: S. Neil Rasband

Signature: \_\_\_\_\_

Signature: \_\_\_\_\_

## Abstract

As applications for extreme ultraviolet (EUV) radiation have been identified, the demand for better optics has also increased. Thorium and thorium oxide thin films (19 to 61 nm thick) were RF-sputtered and characterized using atomic force microscopy (AFM), spectroscopic ellipsometry, low-angle x-ray diffraction (LAXRD), x-ray photoelectron spectroscopy (XPS), and x-ray absorption near edge structure (XANES) in order to assess their capability as EUV reflectors. Their reflectance and absorption at different energies were also measured and analyzed at the Advanced Light Source in Berkeley. The reflectance of oxidized thorium is reported between 2 and 32 nm at 5, 10, and 15 degrees from grazing. The absorption coefficient of the complex index of refraction,  $\beta$ , is also reported between 12.5 and 18 nm. Thin films of thorium were found to reflect better between 6.5 and 9.4 nm at 5 degrees from grazing than all other known materials, including: iridium, gold, nickel, uranium dioxide, and uranium nitride. The measured reflectance does not coincide with reflectance curves calculated from the Center for X-Ray Optics (CXRO) atomic scattering factor data. We observe large energy shifts of up to 20 eV, suggesting the need for an update of the tabulated optical constants.

## **Acknowledgments**

I foremost thank my advisor, Dr. Allred, for the tremendous amount of time he put in to make this project a success. I also thank Dr. Turley for his valuable assistance. The BYU physics department provides an excellent opportunity by involving its undergraduates in research, and I'm grateful to have benefited from it. My fellow group members were very helpful and competent. Much of the credit for this finished thesis goes to them.

## CONTENTS

LIST OF FIGURES .....	v
LIST OF TABLES .....	vii
CHAPTER I. INTRODUCTION.....	1
1.1 Why Mirrors in the EUV?.....	1
1.2 Theory of EUV Reflection.....	2
1.3 Previous Group Research.....	5
1.4 Possible Alternative: Thorium .....	6
1.5 Predictions and Calculations.....	7
CHAPTER II. EXPERIMENTAL.....	10
2.1 Film Deposition .....	10
2.2 Film Characterization.....	14
2.2.1 X-Ray Diffraction .....	14
2.2.2 Energy Dispersive X-Ray Analysis .....	17
2.2.3 X-Ray Photoelectron Spectroscopy .....	19
2.2.4 X-Ray Absorption Near Edge Structure (XANES) .....	22
2.2.5 Atomic Force Microscopy .....	25
2.2.6 Transmission Electron Microscopy .....	30
CHAPTER III. REFLECTION AND TRANSMISSION MEASUREMENTS.....	32
3.1 Advanced Light Source.....	32
3.2 Reflectance Data .....	35
3.3 Transmission Data .....	37
3.4 Comparison to Theory .....	39
CHAPTER IV. OPTICAL CONSTANT FITTING .....	44
4.1 Fitting Overview .....	44
4.2 Results and Comparison .....	45
CHAPTER V. CONCLUSIONS .....	47
REFERENCES .....	49

## LIST OF FIGURES

1.1: Reflection and transmission in a multilayer stack .....	2
1.2: Grazing incidence reflection.....	4
1.3: $\beta$ vs. $d$ at 5.6 nm.....	8
1.4: Theoretical reflectance vs. energy of various materials at 10 deg. from grazing.....	9
2.1: Schematic of a basic sputter system .....	11
2.2: The BYU RF sputtering system “Joey.” .....	12
2.3: Orientation of the quartz-crystal thickness monitor .....	13
2.4: XRD run of sample Th003.....	15
2.5: XRD run of sample Th004.....	15
2.6: Theoretical XRD model computed using IMD and optical constants from CXRO..	16
2.7: EDX scan of Th001 .....	18
2.8: Principle behind XPS.....	19
2.9: Ratio of Th to O vs. film depth in Th003 .....	20
2.10: Grain boundary diffusion and oxidation of Th. ....	21
2.11: XPS of Th001 at the top of the film.....	21
2.12: XPS of Th004 at a depth midway through the sample .....	21
2.13: XPS of Th004 towards the bottom of the sample.....	22
2.14: Experimental setup of a XANES measurement.....	23
2.15: Comparison of Th and U XANES data from 66-100 eV.....	24
2.16: Comparison of Th and U XANES data from 270-310 eV.....	25
2.17: Diagram of the AFM system .....	26
2.18: Low and high frequency roughness compared .....	26
2.19: The effect of surface roughness on reflectance .....	28
2.20: RMS roughness related to length scale.....	28
2.21: The power spectral density of Th003 .....	30
2.22: TEM image of thorium .....	31
3.1: Beamline 6.3.2 schematics.....	32
3.2: Overview of synchrotron operation .....	33
3.3: Reflectometer schematic.....	33
3.4: Reflectance of Th001 vs. wavelength at 5, 10, and 15 deg from 2 to 32 nm .....	35
3.5: Reflectance of Th001 and ThO2_1 vs. wavelength at 5, 10, and 15 deg. from 12.5 to 18.0 nm .....	36
3.6: Measured reflectance of Th001, UO2, UN, NiO on Ni, Ir, and Au vs. wavelength at 5 degrees from 2 to 12 nm .....	37
3.7: Reflection and transmission of Th003.....	38
3.8: Measured absorption coefficient $\beta$ vs. CXRO data as a function of wavelength. ....	39
3.9: Measured (Th001) and computed reflectance of thorium at 10 deg. from 2 to 32 nm .....	40
3.10: Measured (Th001) and computed reflectance of thorium at 10 deg. from 70 to 120 eV.....	41

3.11: Measured (Th001) and computed reflectance of thorium at 10 deg. from 100 to 300 eV .....	41
4.1: Transmission data and fit as a function of angle at 13.9 nm .....	45

## LIST OF TABLES

2.1: Film thickness as determined by XRD .....	17
2.2: XPS identification peaks.....	19
2.3: Lattice spacings of Th.....	31
4.1: Optical constants obtained from transmission data fits at 13.9 and 17.0 nm .....	46
4.2: Comparison of two methods of beta determination.....	46

## **CHAPTER I. INTRODUCTION**

### **1.1 Why Mirrors in the EUV?**

The EUV (extreme ultraviolet) is a portion of the electromagnetic spectrum ranging from about 10-100 nm. While the science of designing mirrors has been well defined for decades in the visible light range, technological limitations and lack of interest have restricted progress in the EUV. Recently, however, potential applications of EUV mirrors have stimulated new research.

Computer chips are fabricated through a process known as optical lithography. Even though improvements in technique have allowed chips to become smaller, optical lithography is limited by the resolution of large optical wavelengths. Shorter EUV wavelengths are capable of finer etching, leading to much faster chips. One of the main problems in harnessing this technology is developing optics with sufficiently high reflectance. [1]

The biological community is also beginning to recognize applications for EUV radiation. Living material is generally more fragile and sensitive to high energy photons. The soft x-ray/extreme ultraviolet range seems to be promising in that it balances higher resolution with the delicateness of organic structures. Sample preparation is another advantage of soft x-ray imaging. Because carbon is opaque and water is relatively transparent from 2.4 to 4.4 nm, cells can be imaged in their native environment without dehydration or staining. [2]

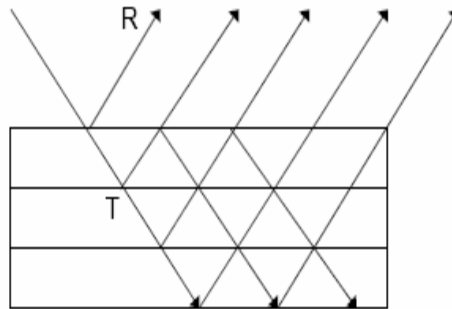
Astronomers have found uses for EUV optics. Members of the BYU XUV research group have participated in designing optics for the EUV instrument on the

IMAGE (Imager for Magnetopause-to-Aurora Global Exploration) satellite. [3] It was designed to provide continuous images of the magnetosphere of the earth by viewing 30.4 nm light from singly ionized He atoms. Other distant astronomical phenomena could also be more effectively studied with better optics. [4]

## 1.2 Theory of EUV Reflection

Designing reflective surfaces in the EUV requires an understanding of the interaction between light and the material. When electromagnetic radiation is incident on a surface, it can either be reflected, transmitted, or absorbed. This is mathematically expressed as:

$$R + T + A = 1. \quad (1.1)$$



**Figure 1.1: Reflection and transmission in a multilayer stack. [4]**

The complex index of refraction, a frequency-dependent property, can be used to predict how light will behave in a material. It is given by

$$N = n + ik, \quad (1.2)$$

where  $n$  is the real part of the index of refraction and  $k$  is the imaginary part, or absorption coefficient. The real part is best understood conceptually as [5]:

$$n = \sqrt{\frac{\mathbf{em}}{\mathbf{e}_0 \mathbf{m}_0}}. \quad (1.3)$$

- $\mu_0$  = permeability of free space
- $\mu$  = permeability of the medium
- $e_0$  = permittivity of free space
- $e$  = permittivity of the medium

Because values of  $n$  in the EUV are so close to unity, it is traditional to express them in terms of a related quantity,  $\delta$ , as shown:

$$\mathbf{d} = 1 - n. \quad (1.4)$$

It is also conventional to use  $\beta$  instead of  $k$ :

$$\mathbf{b} = k. \quad (1.5)$$

If the complete complex index of refraction of a material is known, the reflection from an arbitrary multilayer stack can be computed. The Fresnel coefficients for s and p polarized light are first calculated [6]:

$$f_{p,m} = \frac{N_{m-1}^2 q_m - N_m^2 q_{m-1}}{N_{m-1}^2 q_m + N_m^2 q_{m-1}} \quad \text{and} \quad f_{s,m} = \frac{q_m - q_{m-1}}{q_m + q_{m-1}}, \quad (1.6)(1.7)$$

where  $m$  is the  $m$ th interface in the stack and  $q$  is given by:

$$q_m = \sqrt{N_m^2 - \cos^2 \theta_m}. \quad (1.8)$$

Applying Snell's Law to each interface in the stack, we see that  $N \cos(\theta)$  is constant in each layer. Before the ray has entered the stack,  $\theta_m$  represents the incident angle from grazing as shown in figure 1.2.

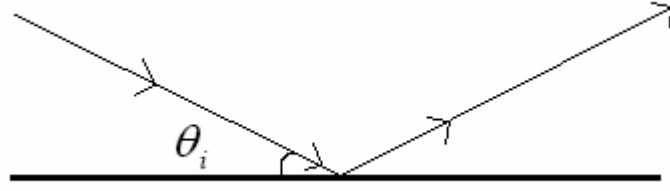


**Figure 1.2: Grazing incidence reflection.**

The recursive Parratt formula is then applied to the Fresnel coefficients in the following manner [7]:

$$r_{s,m} = C_m \frac{f_{s,m} + r_{s,m-1}}{1 + f_{s,m} r_{s,m-1}} \text{ and } r_{p,m} = C_m \frac{f_{p,m} + r_{p,m-1}}{1 + f_{p,m} r_{p,m-1}}, \quad (1.9)(1.10)$$

where

$$C_m = e^{-iq_m z_m / l_m}. \quad (1.11)$$

- $q$  = wavenumber in layer
- $z$  = layer thickness

From these values, the reflection of any layer of the stack can be easily calculated:

$$R_s = |r_{s,M}|^2 \text{ and } R_p = |r_{p,M}|^2. \quad (1.12)(1.13)$$

The complex index of refraction can also be written in terms of the dielectric constant [8]:

$$N^2 = \mathbf{e} = \mathbf{e}_1 + i\mathbf{e}_2 \quad (1.14)$$

Separating  $e_1$  and  $e_2$  into real and imaginary components yields:

$$\mathbf{e}_1 = (1 - \mathbf{d})^2 - \mathbf{b}^2 \quad (1.15)$$

$$\mathbf{e}_2 = 2(1 - \mathbf{d})\mathbf{b}. \quad (1.16)$$

Because of the difficulties associated with tabulating optical constants in the EUV, the atomic scattering factor approach was developed to predict them. The atomic scattering factor,  $f$ , is defined as [9]:

$$f = f_1 - if_2, \quad (1.17)$$

where  $f_1$  and  $f_2$  are related to the optical constants as follows:

$$f_1 = \frac{2p}{n_a r_e \lambda^2} \mathbf{d} \quad (1.18)$$

$$f_2 = \frac{2p}{n_a r_e \lambda^2} \mathbf{b} \quad (1.19)$$

- $n_a$  = atomic density
- $r_e$  = classical electron radius ( $2.82 \times 10^{-15}$  m)
- $\lambda$  = wavelength in vacuum

The atomic scattering factors of a material can be calculated using the Lorentz-Drude model. It can be seen after a number of calculations and approximations that the atomic scattering factor is equal to the density of electrons in a material. [9] Reflectance results from light's interaction with electrons. Consequently, heavier elements with many electrons, such as uranium, generally exhibit higher reflectance.

### 1.3 Previous Group Research

Since the late 1990's, the BYU thin films research group has conducted reflectance experiments with uranium-coated mirrors. Because of its high atomic number and density, the scientific community had identified uranium as an element which would theoretically be useful in preparing coatings with high reflectance in the soft x-ray and extreme ultraviolet range.

Though uranium is still very promising and continues to be studied, there are major obstacles associated with its use. Uranium oxidizes fairly easily in its elemental form and has many oxidation states. When exposed to oxygen, elemental uranium will tarnish, first forming  $\text{UO}_2$ , and later higher oxides such as  $\text{U}_2\text{O}_5$  and  $\text{UO}_3$ . This critical characteristic complicates its practical use and makes optical property measurements difficult. When exposed to air for only a matter of minutes, a fresh uranium surface rapidly oxidizes to a depth of more than 10 nm, changing the composition of the top portion of the thin film and dramatically lowering the EUV/soft x-ray reflectance. [4] As the lighter oxygen atoms are incorporated into the lattice structure, they push apart the uranium atoms that are most effective in reflecting this high energy light. Although at 500 nm a 10 nm thick oxide film would have only a slight effect on uranium's reflectance, at 5 nm the oxide is the dominant reflecting surface. Uranium metal is never the front surface of any uranium-containing mirror used in the EUV or soft x rays, unless it is made and always kept under UHV. How far and how fast the oxidation proceeds depends chiefly on exposure time, temperature, and the ambient environment. The major obstacle this presents is not knowing the exact composition of the film.

#### **1.4 Possible Alternative: Thorium**

This paper focuses on a less problematic alternative to uranium. Periodic table neighbor, thorium, is also a fairly stable radioactive metal. Its half-life of 15 billion years is three times that of U-238, the major constituent of depleted uranium. [10,11] The atomic scattering factors of Th and U are expected to be similar over most of the spectrum since the elements have a similar number of electrons. However, thorium's bulk density ( $11.7 \text{ gm/cm}^3$ ) is considerably less than that of uranium ( $19.3 \text{ gm/cm}^3$ ). [10,12]

The large difference in density makes the  $d$  of Th considerably less than U. This is because  $d$  is proportional to density times the real part of the atomic scattering factor. (equation 1.18) For this reason, searches for high  $d$  and  $\beta$  do not turn up Th.

However, thorium cannot oxidize beyond the +4 oxidation state, ThO<sub>2</sub>. [13] In contrast to uranium, other oxidation states are scarcely known. Therefore, we can more accurately determine the compound's theoretical reflectance. While it can still be difficult to predict how deep the oxidized layer runs, we definitely know the composition of our compound. Additionally, this smaller oxidation state translates to less overall oxygen incorporation and a reflectance closer to pure elemental thorium. In fact, whereas uranium is more than 50% denser than thorium metal, bulk UO<sub>2</sub> (10.96 gm/cm<sup>3</sup>) is only about 11% more dense than bulk ThO<sub>2</sub> (9.86 gm/cm<sup>3</sup>). [4,14]

## 1.5 Predictions and Calculations

At an interface, reflection results because of a difference in the optical constants of the two mediums. In vacuum,  $d$  and  $\beta$  are both zero. Therefore, a material with a large  $d$  and  $\beta$  reflects well in vacuum. In fact, reflection at normal incidence can be approximated as [9]:

$$R_{s,p} \cong \frac{d^2 + b^2}{4}. \quad (1.20)$$

A material with a large  $d$  is preferential over a large  $\beta$  because absorption will significantly lower the reflectance of a large multilayer stack. [15] Figure 1.3 shows a scatter plot of  $\beta$  vs.  $d$  for various elements at 5.6 nm. These values were computed using the atomic scattering factors tabulated on the CXRO website. [16]

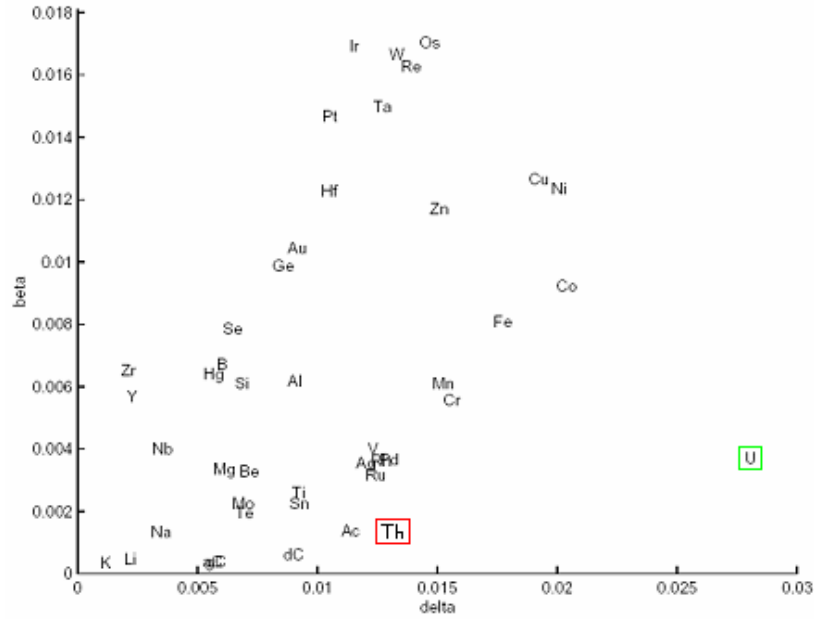


**Figure 1.3:  $\beta$  vs.  $d$  at 5.6 nm. Groups of elements on the periodic table tend to cluster. [3]**

In general, elemental neighbors on the periodic table group together on these scatter plots. This is true because of similarities in number of electrons and density. Although it is expected that uranium and thorium will exhibit similar optical properties, this apparently is not the case. Figure 1.3 shows the large separation in the two circled elements. This is probably due to a large difference in density. Nevertheless, this issue warrants experimental verification and examination.

These CXRO data can be used to calculate theoretical reflectance at various angles and energies. Figure 1.4 compares the reflectance of uranium and thorium with two common EUV reflectors, nickel and gold. The oxides of both thorium and uranium are plotted because inevitably the original metallic films will oxidize. In calculating the optical constants and reflectance of compounds, the elemental atomic scattering factors are weighted according to their relative abundance. The density of the compound is also

figured in. No modification is made to the theory to account for bonding or a change in lattice structure. [9] This introduces a problem which will be discussed in further detail in chapter 3.

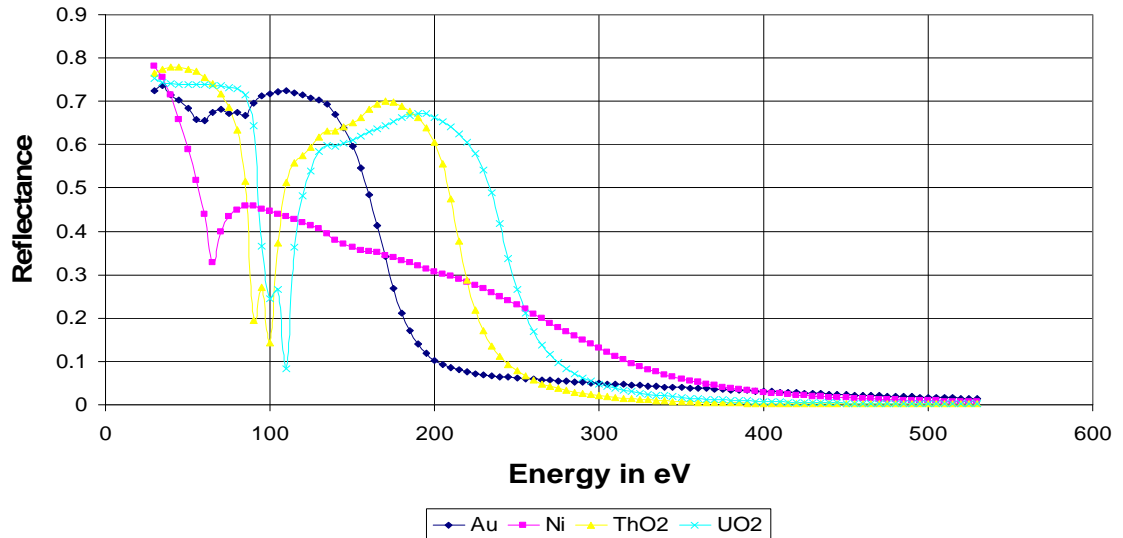


**Figure 1.4: Theoretical reflectance vs. energy of various materials at 10 deg. from grazing.**

The graph shows that thorium could potentially reflect well over a number of ranges. There are even certain energies where it could be the best reflector of any known material. Even though uranium appears to be the better alternative, further oxidation will decrease the density of the film and lower its reflectance. This should be less of an issue with thorium.

## CHAPTER II. EXPERIMENTAL

### 2.1 Film Deposition

Thin film samples were RF-magnetron sputtered in a deposition system built at BYU. A four-inch target is mounted on a US Inc. sputter gun in a sputter-up geometry. The target is the material which will be coated onto the substrate. The distance between the target and the sample is about 0.3 m. In a typical sputtering deposition, the chamber was evacuated to a base pressure between  $6 \times 10^{-5}$  to  $1.3 \times 10^{-4}$  Pa, often starting with a 1-hr bake-out. A Cryotorr-8 cryopump was used to establish the base pressure of the system. A small turbo pump was used in parallel with the cryopump to remove hydrogen and helium, which are not pumped well by the cryopump. The system, which employs copper gaskets, has been capable of ultrahigh vacuum pressures of less than  $10^{-5}$  Pa when all incoming gas lines are leak free. Using a Ferran Scientific Millipole Analyzer (MPA), it was determined that the argon line had a minute air leak. The MPA indicated a residual gas composition in the system consistent with that of air. Analysis of samples using XPS (x-ray photoelectric spectroscopy) showed no significant nitrogen content. At our base pressure, only ambient oxygen at a partial pressure of about  $2 \times 10^{-5}$  Pa was able to incorporate slightly into sputtered samples.

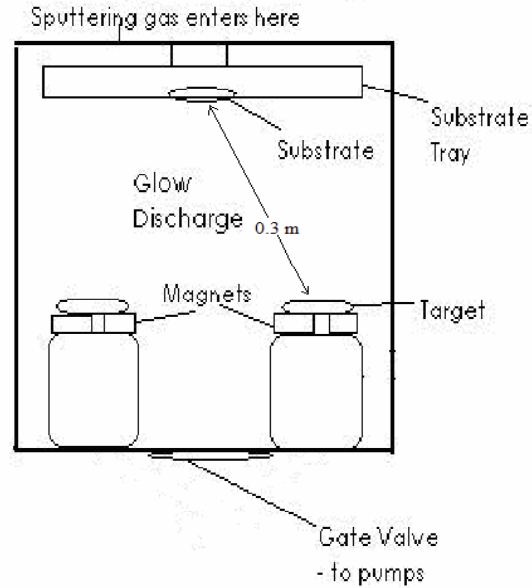


**Figure 2.1: Schematic of a basic sputter system. [4]**

Before deposition, the gate valve to the cryopump was throttled to about one-quarter open. Then, argon was introduced to the system and adjusted using a 20-sccm mass flow controller to the desired working pressure (0.1 to 11 Pa). When this was achieved, an RF voltage was applied between the target and a grounded housing. The impedance of the system was also adjusted to approximate that of the chamber, lowering the reflected power and maximizing power efficiency. The induced potential difference ionizes the argon atoms and creates a glowing purple plasma in the chamber. Strong magnets directly underneath the target confine the plasma to the region right above it. This concentrating of atoms allows the overall sputtering pressure to be lower, increasing the mean free path. Less collisions between atoms lead to a higher deposition rate. An electric field in the chamber accelerates the argon ions towards the target with enough kinetic energy to knock atoms off the surface of the target. This continual bombardment creates an effective spray of target atoms which coats anything unobstructed. [15]

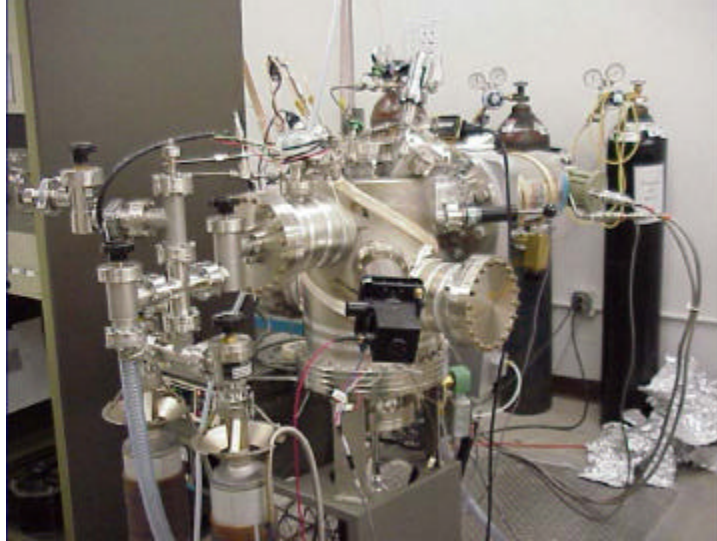


**Figure 2.2: The BYU RF sputtering system “Joey.” [4]**

In addition to increasing the sputtering rate, a higher mean free path allows the target atoms to reach the substrate with more kinetic energy. In fact, at the typical sputtering pressure, the mean free path was as high as 3 cm, a factor of 750,000 greater than atmospheric conditions. The overall benefit is a smoother, denser, more continuous film with fewer irregularities.

A closed shutter below the substrates kept sputtered atoms from reaching the substrate while the sputtering conditions were being stabilized. No substrate bias or heating was employed.

ThO<sub>2</sub> thin films were reactively sputtered by flowing oxygen through a separate line into the chamber. The flow rate was controlled by a low-flow sapphire-diaphragm valve immediately above the chamber. Before igniting the plasma, the argon and oxygen flows were independently set so that oxygen would constitute about 20% of the gas atoms. The deposition rates of thorium and thorium oxide, respectively, were usually

about 0.2 and 0.02 nm/sec. The diminished sputter rate in the case of ThO<sub>2</sub> is thought to be due to substantial poisoning of the target surface with oxygen.

The initial estimate of the film thickness was determined using a quartz-crystal thickness monitor which sits in front of the shutter and slightly to the side of the chamber. Consequently, the monitor is further from the target and at a smaller solid angle to it, resulting in a smaller film thickness. The concentration of sputtered material is also angle dependent, compounding this issue. These estimates of the thickness also depend on a manual density input, which is not always the same as the handbook (bulk) density. A tooling factor can be calculated from alternate methods of thickness measurement to correct for these problems. These techniques will be discussed later.

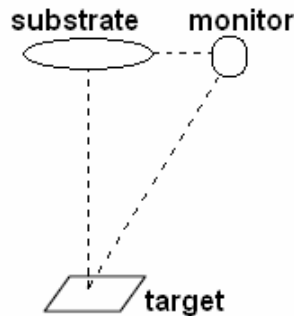


**Figure 2.3: Orientation of the quartz-crystal thickness monitor. [15]**

Several different substrates [including silicon wafer pieces, fused quartz slides, thin polymer windows, and carbon-coated TEM (transmission electron microscopy) grids] were coated simultaneously so that the deposited films could be studied by multiple characterization techniques. The substantial substrates (Si and quartz) were cleaned using methanol and helium to remove surface contaminants prior to the deposition.

## 2.2 Film Characterization

One of the most significant challenges in thin film research is determining the exact characteristics of a deposited film. This is critical because optical constant measurements depend on quantities such as thickness, elemental composition, and roughness. The following section will detail the techniques and data obtained from our characterization methods.

### 2.2.1 X-Ray Diffraction

Low angle x-ray diffraction (LAXRD) was employed to determine film thickness. Cu-K<sub>a</sub> x rays at 0.154 nm produced by a Cu rotating anode source are directed at the sample, which is moved between 0.4 and 3 degrees from grazing while a detector, placed at twice the sample angle, records the reflected intensity. Evenly spaced peak and valleys are present in the plot because of repeating constructive and destructive interference fringes. Local maxima can be approximated using the Bragg Equation:

$$m\lambda = 2d \sin(\theta) \quad (2.1)$$

- $\lambda$  = wavelength in the material
- $d$  = film thickness
- $m$  = integer
- $\theta$  = incident angle from grazing

The film thickness  $d$  can be estimated because wavelength and angle are known. This formula is only included as background, and it suffers considerably when the peak heights are strongly damped.

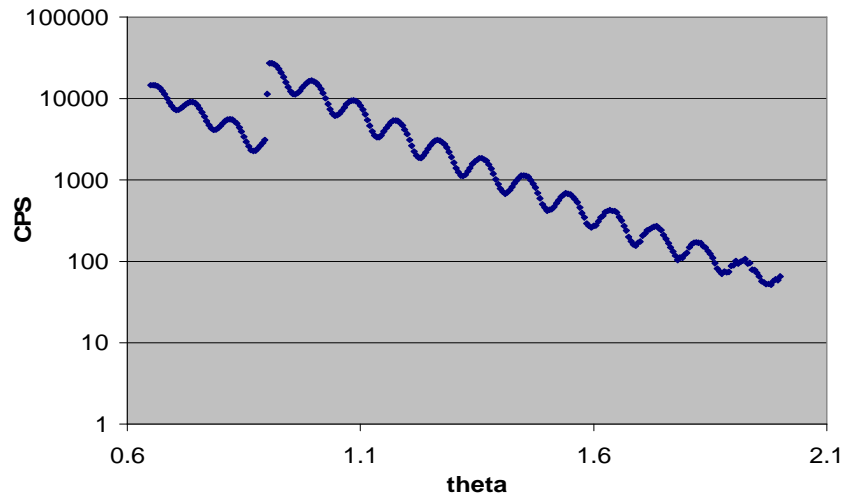


**Figure 2.4: XRD run of sample Th003.**

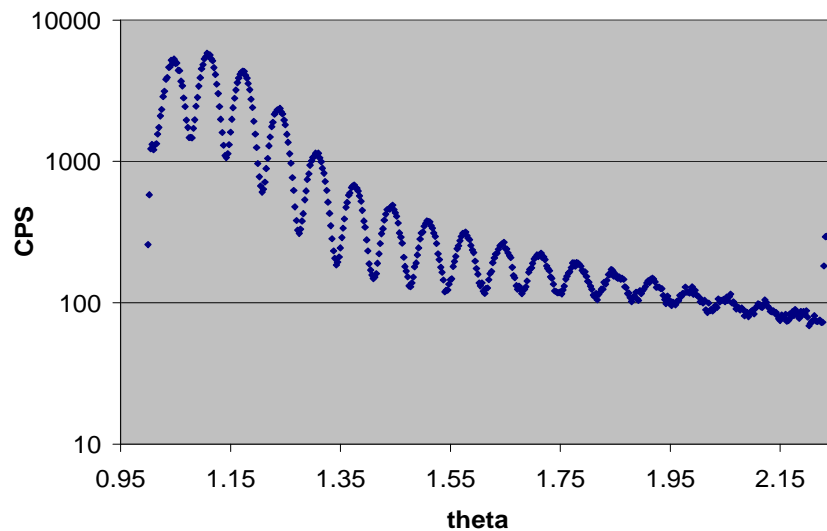


**Figure 2.5: XRD run of sample Th004.**

The x-axis “theta” in the two graphs refers to the angle of the sample stage, not the detector. An abrupt jump can be seen in the figure 2.4 graph at about 0.9 degrees. This happens when the incident intensity of the x rays is manually changed by the user to increase the gain.

A model is created in order to fit for the thickness of a sample using XRD plots. We used Dave Windt's IMD program [17] to theoretically model the XRD patterns of thorium. The program uses calculated optical constants from CXRO to predict reflection spectra at varying energies and angles. The films were approximated as layers of pure thorium capped with 5 nm of thorium dioxide to account for natural oxidation. The separation in angle between 8 minima was counted for each thickness and was plotted as thickness vs. delta theta. This curve was then fit with a third order polynomial, rendering an equation for thickness as a function of the angular difference between 8 peaks centered around 1.5 degrees. Armed with this knowledge, thickness can be extracted from any thorium XRD data.

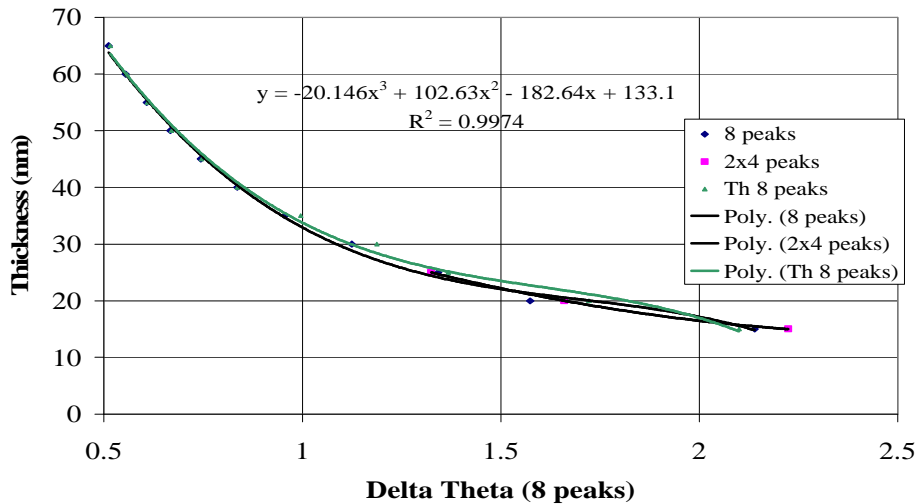


**Figure 2.6: Theoretical XRD model computed using IMD and optical constants from CXRO.**

Other fitting methods using XRD to obtain thickness values were not performed. Experience has shown that thicknesses calculated in this manner differ by only 2-3%. Thickness accuracy was not crucial for the purposes of this thesis because only

preliminary optical constants at two wavelengths are reported. These measurements will soon need to be verified, however, as group members are currently working on optical constant fitting at additional wavelengths. XRD fit programs and ellipsometry are two ways these preliminary film thicknesses can be refined.

Sample	XRD Thickness
Th001	19.7 nm
Th002	47.5 nm
Th003	46.0 nm
Th004	61.6 nm
ThO2_1	44.1 nm

**Table 2.1: Film thickness as determined by XRD.**

XRD measurements of several samples were made immediately after the samples were removed from the sputter system. Follow up measurements were also performed to gauge the rate of thickness expansion over time. The data has not been quantitatively analyzed yet, but the oxidation rate of thorium looks to be slower than that of uranium. [15,18] The XRD thickness of the examined films increases monotonically, though gradually slower, with time. I associate this change with oxidation. Analysis and further study are needed.

### **2.2.2 Energy Dispersive X-Ray Analysis**

Energy dispersive x-ray analysis (EDX) is a tool similar to XPS. It differs in that it sees through the entire sample and is not simply a surface scan. An electron beam in the range of 10-20 keV hits the sample, which stimulates the emission of x rays. These x rays emanate everywhere from the surface down to 2 microns deep. [19] Each element emits a

characteristic x-ray spectrum which is captured by a detector and used for identification.

Figure 2.7 shows the EDX data of Th001. The large covered peak near 1.8 eV is Si.

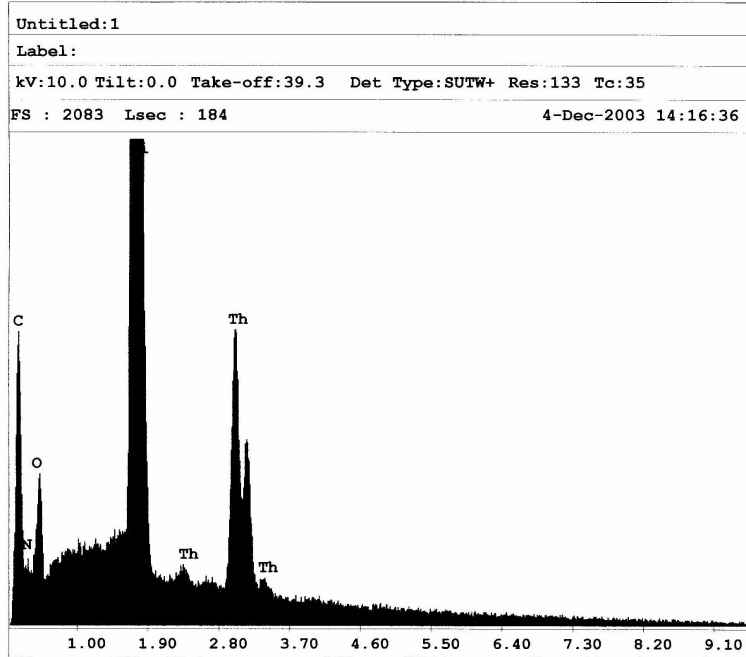


Figure 2.7: EDX scan of Th001.

Much of what we see is expected. No other contaminant metals are present. There are prominent thorium peaks along with an oxygen peak which is consistent with film oxidation. The small amplitude of the nitrogen peak confirms some minimal contamination during sputtering. There is an unexpectedly large carbon peak which merits further analysis. Possible explanations include residue cutting fluid sputtered from the target, airborne hydrocarbon contaminants, or even the chance that our target is thorium carbide. This will be later addressed in chapter 3.

### 2.2.3 X-Ray Photoelectron Spectroscopy

X-ray photoelectron spectroscopy (XPS) was used to determine the composition depth profiles of the samples at various depths. Particular attention was given to oxygen and other impurities. As the film was sputtered through, incident x-rays were directed at the film. XPS uses the photoelectric effect, which is given by:

$$K_e = hf - \phi \quad (2.2)$$

- $K_e$  = kinetic energy of ejected electron
- $h$  = Planck's constant
- $f$  = frequency of incident light
- $\phi$  = work function

Depending on the measured energy of ejected electrons, the binding energies of certain states can be calculated. The intensity and energy of these electrons respectively determine relative elemental abundance and how the atoms are bonded. Generally, as a metal is oxidized, the remaining electrons are bound more tightly. This is seen as a peak position shift of about 2 eV to higher energy as oxygen content increases.

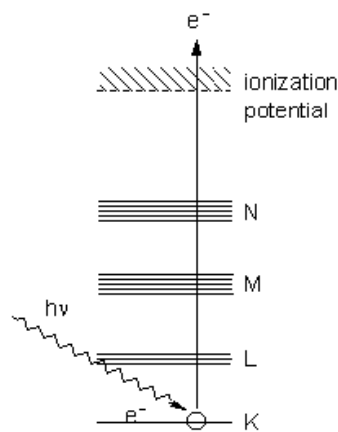
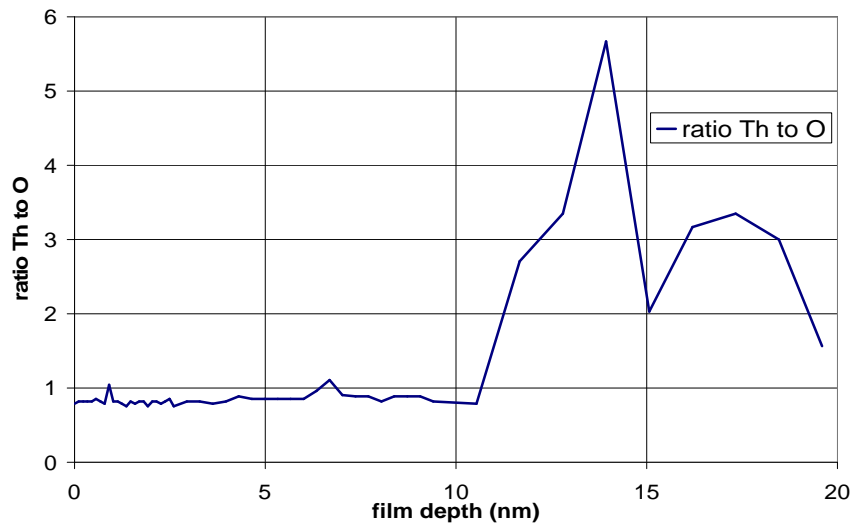


Figure 2.8: Principle behind XPS. [20]

Scan of Surface Identifying Peaks:	
177eV	– Th 5p <sub>3/2</sub>
234eV	– Th 5p <sub>1/2</sub>
280eV	– C 1s
294eV	– Th 5s
333eV	– Th 4f <sub>7/2</sub>
342eV	– Th 4f <sub>5/2</sub>
398eV	– N 1s
530eV	– O 1s
676eV	– Th 4d <sub>5/2</sub>
713eV	– Th 4d <sub>3/2</sub>
980eV	– Auger O Line

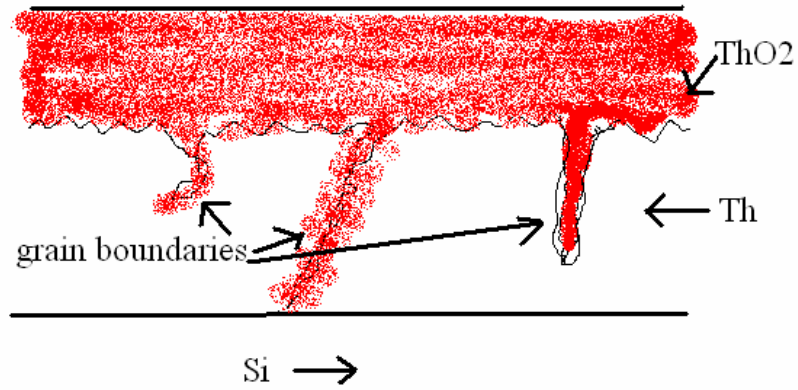
Table 2.2: XPS identification peaks. [21]

These principles can be applied to study film oxidation. Figure 2.9 shows the ratio of thorium content to oxygen in the 19.7 nm Th003 film. The film has oxidized mostly to ThO<sub>2</sub> through the first 10 nm. After that, there is a sharp increase in thorium concentration. The presence of oxygen past 10 nm, however, indicates either a limited amount of oxidation or oxygen contamination during sputtering. The substrate begins to appear around 17 nm.

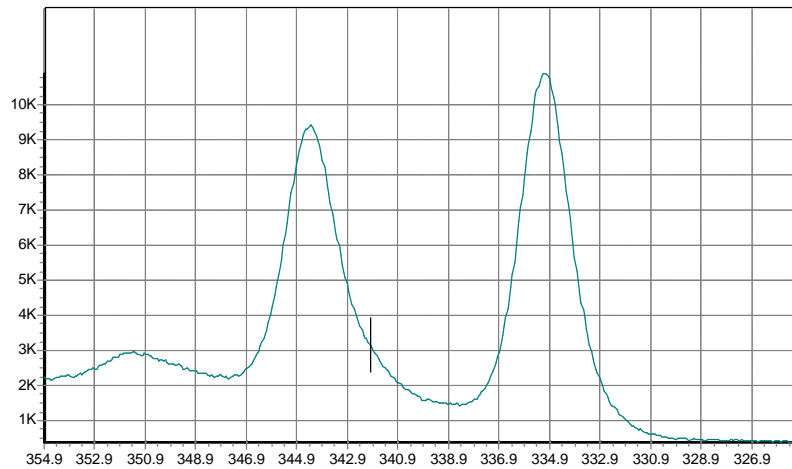


**Figure 2.9: Ratio of Th to O vs. film depth in Th003. [22]**

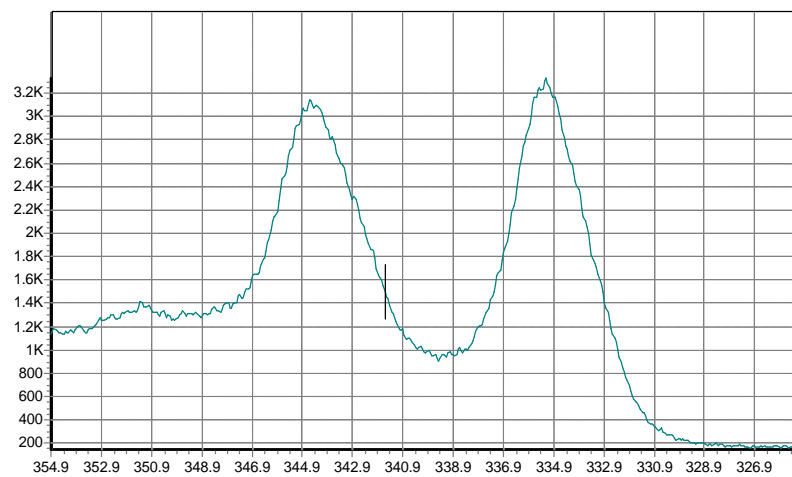
Figure 2.9 alone does not clarify the exact nature of the oxidation. Analysis of figures 2.11-2.13 can be used to determine whether the oxygen content represents a thorium monoxide intermediate oxidation state or regions of thorium dioxide interspersed in the metallic thorium. Grain boundaries and film imperfections could allow for the regional oxidation of the film.



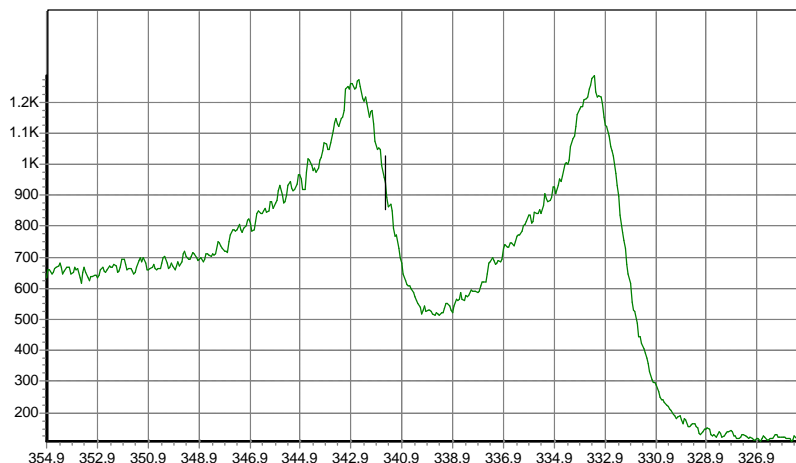
**Figure 2.10: Grain boundary diffusion and oxidation of Th.**



**Figure 2.11: XPS of Th001 at the top of the film. [22]**



**Figure 2.12: XPS of Th004 at a depth midway through the sample. [22]**



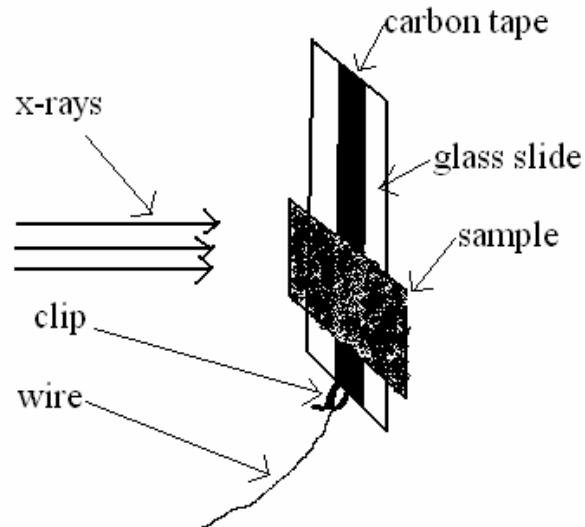
**Figure 2.13: XPS of Th004 towards the bottom of the sample. [22]**

Figure 2.11 is a surface scan of Th001. Its lower energy peak is very close to the literature value of 334.4 eV. On the other hand, figure 2.13 shows the bottom of thorium sample Th004. The lower peak matches well with the literature value of 333.2 eV for thorium metal. [21] We interpret the shoulders at the high energy side of these peaks as belonging to a thorium oxide, which is probably ThO<sub>2</sub>. Figure 2.12 is the XPS spectrum of Th004 halfway down, in the region where the oxygen to thorium ratio is about 1. We note that the full width at half max of these peaks is noticeably larger than figure 2.11 or 2.13. This is interpreted to be regions of both Th and ThO<sub>2</sub> at this intermediate depth. A single phase of ThO could be expected to show a peak as narrow as Th or ThO<sub>2</sub>. Its position, though, would be in the middle of them.

#### **2.2.4 X-Ray Absorption Near Edge Structure (XANES)**

XANES is an experimental technique which was used for the first time by the group in March 2004. A piece of carbon tape is placed on a glass slide and the sample is secured so that it is contacting the tape. A clip with a wire leading to a detector is then

attached to the end of the carbon tape. As x rays encounter the sample, core electrons are excited into unoccupied states. This stimulation produces a signature current depending on the energy of the x rays and the properties of the sample. Measurements are also taken off the carbon tape to provide a reference for normalization.



**Figure 2.14: Experimental setup of a XANES measurement.**

XANES can provide information about vacant orbitals, electronic configuration, and site symmetry of the absorbing atom. The absolute position of the edge contains information about the oxidation state of the absorbing atom. In the near edge region, multiple scattering events dominate. Theoretical multiple scattering calculations are compared with experimental XANES spectra in order to determine the geometrical arrangement of the atoms surrounding the absorbing atom. [23]

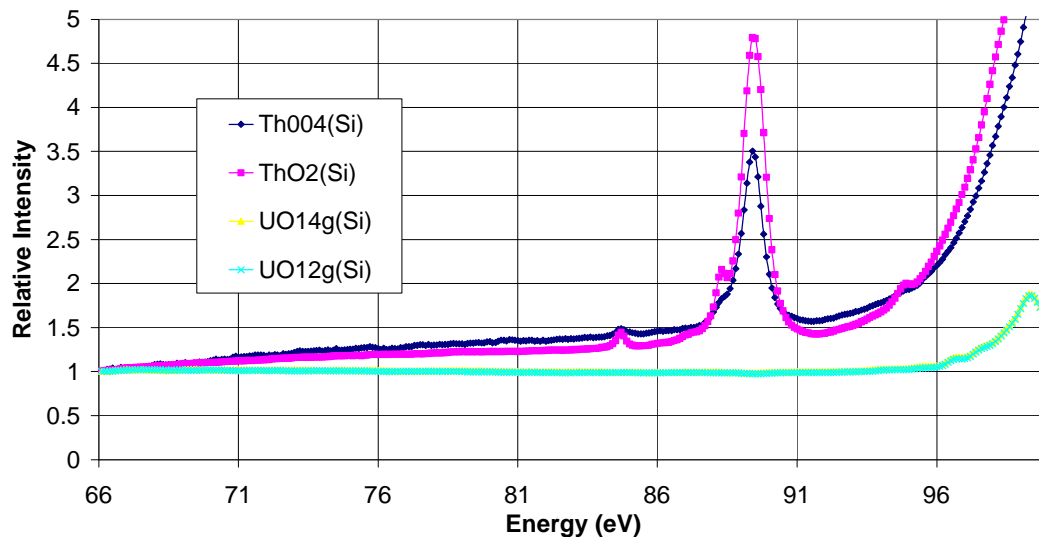


**Figure 2.15: Comparison of Th and U XANES data from 66-100 eV.**

The low energy XANES data presented in figure 2.15 shows an absorption peak close to 89 eV. The uranium samples serve as a reference to make sure our normalization techniques are sound. The absence of a large peak at 89 eV for uranium makes it likely that the feature is unique to thorium. It is probably not oxygen because the oxygen atoms in the uranium film would also contribute similar absorption.

Figure 2.15 contains a number of subtle features which denote differences in the optical properties of thorium and thorium oxide thin films. There are small absorption differences near 84, 88, and 95 eV. Presumably these peaks are due to the differences in the binding energies of electrons in the oxide.

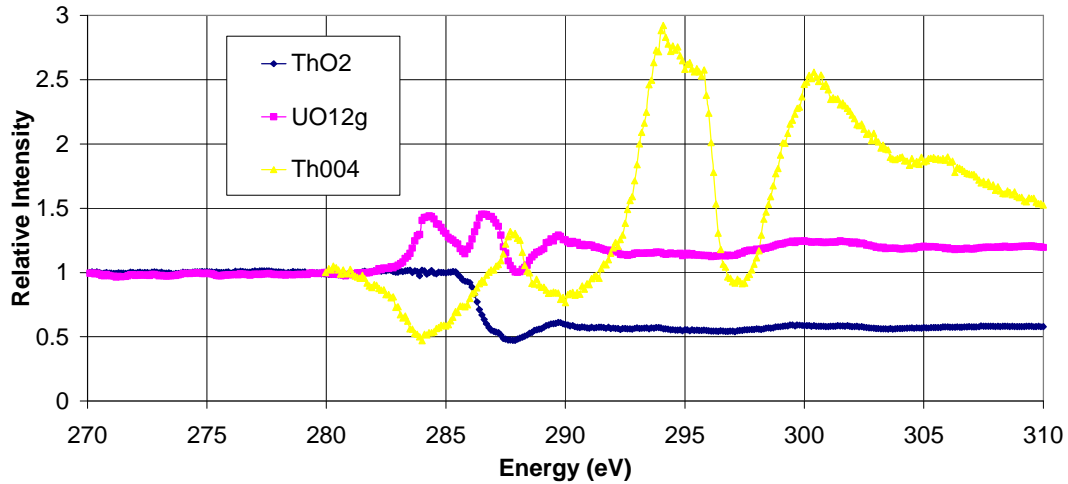


**Figure 2.16: Comparison of Th and U XANES data from 270-310 eV.**

Additional XANES data are presented in figure 2.16. A uranium dioxide sample is again included to serve as a comparison. Immediately apparent is the dramatic difference in the two thorium curves. We are fairly confident in the high oxygen content of the thorium dioxide film because the sample on quartz is visibly transparent. The degree of natural oxidation of the Th film, however, is unclear. While it would be intuitive to assume similarity in the XANES curves of the two films, this is not the case. Lattice structure and elemental ratios presumably play a large role in this data.

### **2.2.5 Atomic Force Microscopy**

AFM is used for imaging surfaces at the nanometer scale. A small tip attached to a cantilever is dragged across the surface to be probed. The tip is deflected slightly as it encounters features on the surface. In order to detect these small displacements, a laser is first aligned so that it reflects off the cantilever and into a photodiode detector. The photodiode is subdivided into regions which precisely measure laser intensity. Any small

change in the cantilever's angle will cause the laser to be reflected differently into the photodiode. The intensity pattern changes and this is digested as physical data.

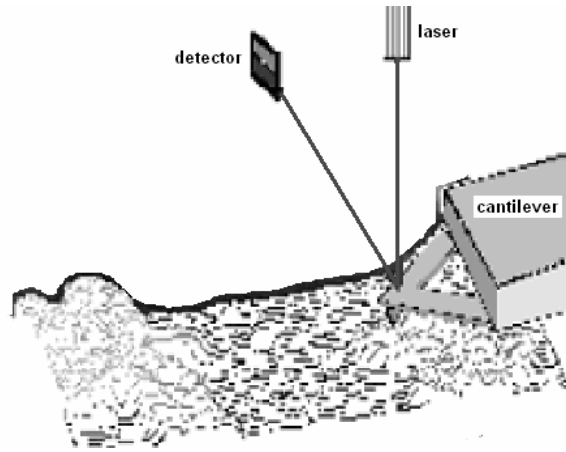


**Figure 2.17: Diagram of the AFM system. [24]**

AFM was used to measure the roughness of our samples. This is important because surface roughness lowers the reflectance of thin films and complicates the calculation of optical constants. Large scale, or low frequency roughness, results in beam scattering. Diffraction effects accompany small scale, or high frequency roughness. [25] These factors arise from the imperfect nature of both the substrate and the deposition techniques.

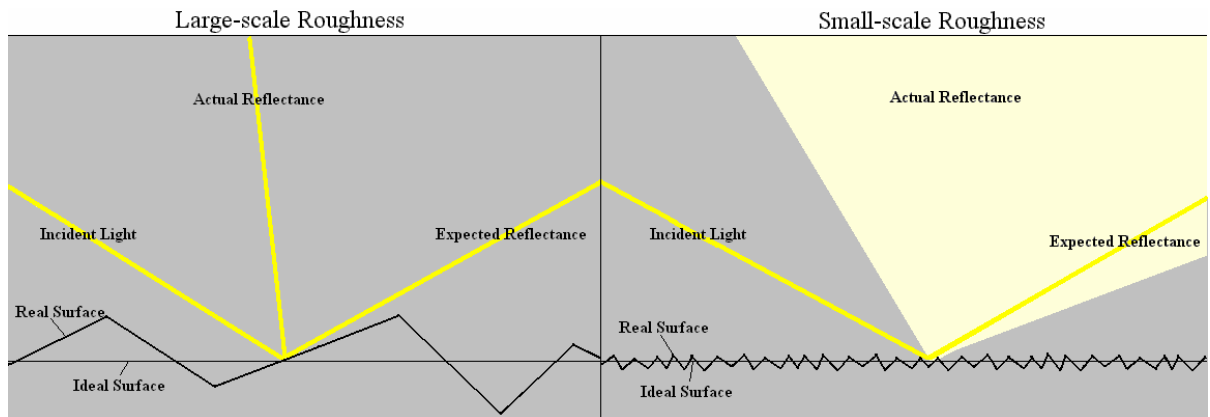


**Figure 2.18: Low and high frequency roughness compared. [25]**

There are a number of models which attempt to integrate roughness into theoretical data. The Debye-Waller method is given by [26]:

$$R_s = R_0 e^{-\left(\frac{4ps}{\lambda}\right)^2} \quad (2.3)$$

- $R_s$  = measured reflectance
- $R_0$  = calculated reflectance
- $\lambda$  = wavelength
- $s$  = RMS deviation of surface

This model tends to underestimate the effects of roughness. The Nevot-Croce method is an alternative to Debye-Waller which overestimates the effects. It is represented by [27]:

$$R_s = R_0 e^{-q_1 q_2 s^2} \quad (2.4)$$

- $q_x = \frac{4pn \sin(\theta)}{\lambda}$
- $n$  = real part of complex index of refraction
- $\theta$  = incident angle from grazing

The two models were averaged to estimate the reduction in reflectance due to roughness. This is shown graphically in figure 2.19. The calculated curve shows the reflectance of a completely smooth thorium film at 15 nm. When the effects of roughness are added, there is a drop in reflectance denoted by the “measured” curve.

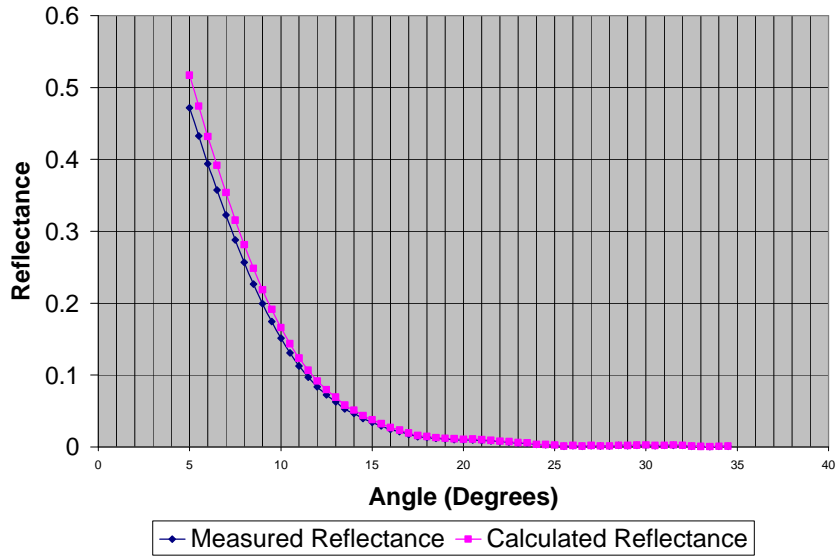


Figure 2.19: The effect of surface roughness on reflectance. [28]

Roughness measurements were made over three different length scales. This refers to the length of the sides of the square area scanned by the AFM tip. Two separate areas from three different samples were scanned and plotted in figure 2.20. The two areas were averaged to form an estimate of the RMS roughness of each sample.

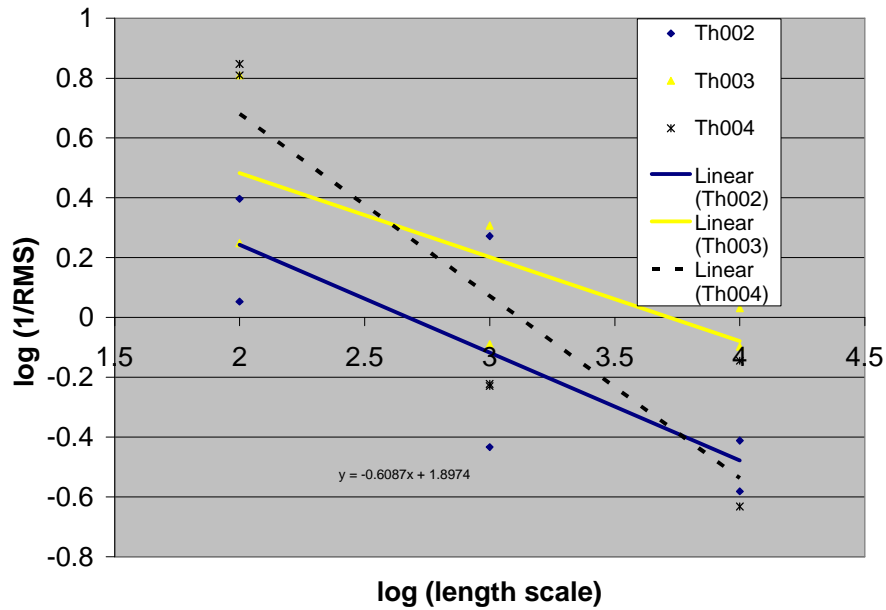


Figure 2.20: RMS roughness related to length scale. [28]

The RMS roughness of a sample goes up as the length scale increases. Roughness should also be more of a factor with thicker samples. Ideally, the linear fits plotted in figure 2.20 would have approximately the same slope. This discrepancy is probably due to randomness related to insufficient sampling. RMS roughness from the three samples can be approximately extracted for any length scale by the following equations:

$$\text{Th002:} \quad \log\left(\frac{1}{RMS}\right) = -0.3607 \cdot \log(\text{length scale}) + 0.9645 \quad (2.5)$$

$$\text{Th003:} \quad \log\left(\frac{1}{RMS}\right) = -0.281 \cdot \log(\text{length scale}) + 1.0446 \quad (2.6)$$

$$\text{Th004:} \quad \log\left(\frac{1}{RMS}\right) = -0.6087 \cdot \log(\text{length scale}) + 1.8974. \quad (2.7)$$

A three dimensional surface plot could be constructed showing roughness as a function of thickness and length scale if enough samples were analyzed.

It is sometimes useful to know whether low or high frequency roughness is more prevalent. The AFM obtains the height and the density of aberrations on the film. Software is capable of performing Fourier analysis on the flattened data to obtain a power spectral density. For our purposes, we identify high frequency roughness to be below  $10 \text{ nm}^{-1}$  and low frequency to be above it. High frequency roughness around the wavelength of the light being reflected will cause the light to scatter in all directions or decrease its intensity. High frequency roughness considerably smaller than the wavelength of light is believed not to have much effect. Low frequency roughness will cause the light to scatter uniformly. It was found that high frequency roughness constituted about 90% of the total. [28]

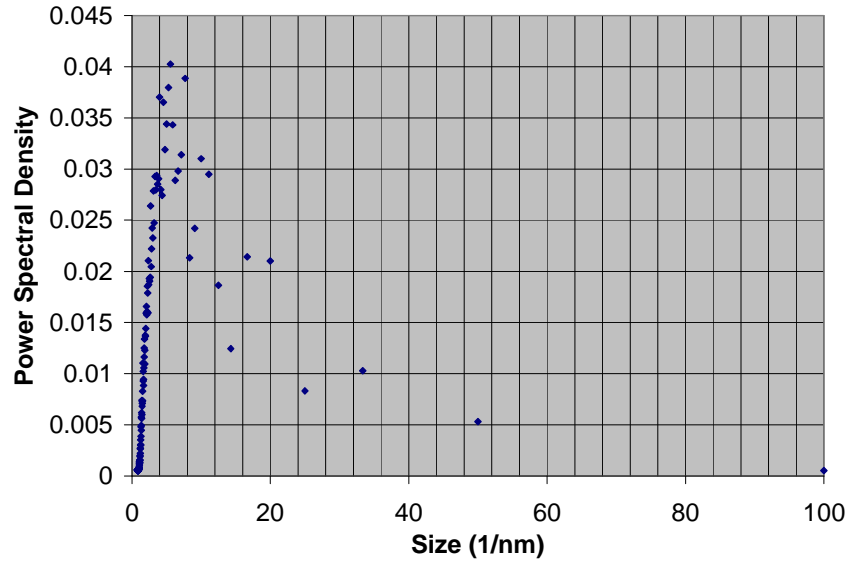
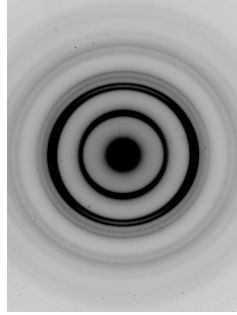


Figure 2.21: The power spectral density of Th003. [28]

### 2.2.6 Transmission Electron Microscopy

TEM is used to determine the lattice spacing and orientation of the atoms in a film. Special substrates called TEM grids are coated during depositions. An electron beam is shot at the coated grid and the transmitted electrons form circular patterns on a phosphorescent screen. The relevant information is deduced from measurements of the radii of these rings. The lattice spacings of three different TEM grids from the same deposition were calculated. The thickness of this sample has not been determined. The average of the three grids and the literature value for face-centered cubic Th agree to within 0.03 ? .



**Figure 2.22: TEM image of thorium. [28]**  
**The scale is about 7 cm from left to right.**

Sample	Lattice Spacing (? )
Th006 TEM1	5.09
Th006 TEM2	5.13
Th006 TEM3	5.12
Th006 Average	5.11
Literature	5.08

**Table 2.3: Lattice spacings of Th. [28,29]**

## CHAPTER III. REFLECTION AND TRANSMISSION MEASUREMENTS

### 3.1 Advanced Light Source

Reflectance measurements were taken on beamline 6.3.2 at the Advanced Light Source in Berkeley, California. A 1.9 GeV synchrotron accelerates electrons close to the speed of light in a circular path using powerful bending magnets which create magnetic fields near 1 T. [30] This produces high intensity radiation from about 30 nm down to 0.2 nm. [31] Tangent offshoots known as beamlines carry the light to the users. The beam on line 6.3.2 happens to be 90% s-polarized and 10% p-polarized. Before being used in experimentation, it passes through a number of components to ensure it is collimated and monochromatic. The monochromator uses a combination of gratings, filters, and order sorters to channel the desired wavelength to the reflectometer, or “scattering” chamber.

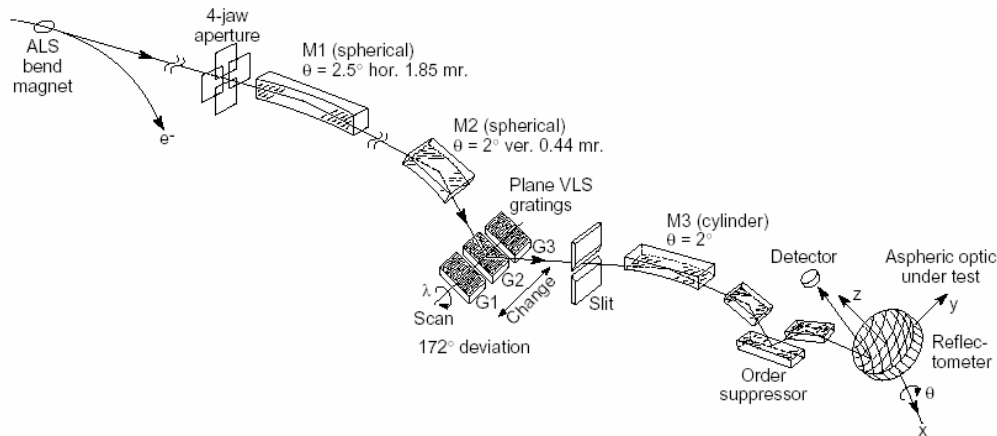


**Figure 3.1: Beamline 6.3.2 schematics. [31]**

Once the beam reaches the reflectometer, the sample is brought into its path and the reflected light is collected by a detector. The sample is mounted on a stage which can be translated in three dimensions and rotated through any incident angle. Either the

wavelength or angle can be scanned while the other remains fixed. There are two detectors available for use. A CCD is employed to locate the position of beam during alignment procedures. A photodiode is then used to measure beam intensity.

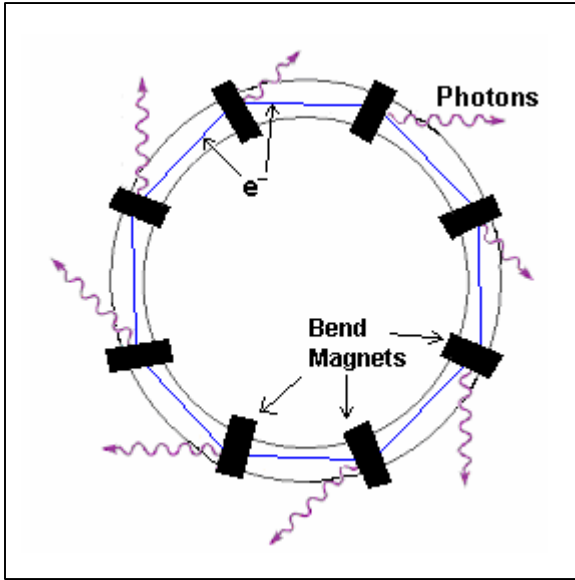


Figure 3.2: Overview of synchrotron operation. [32]

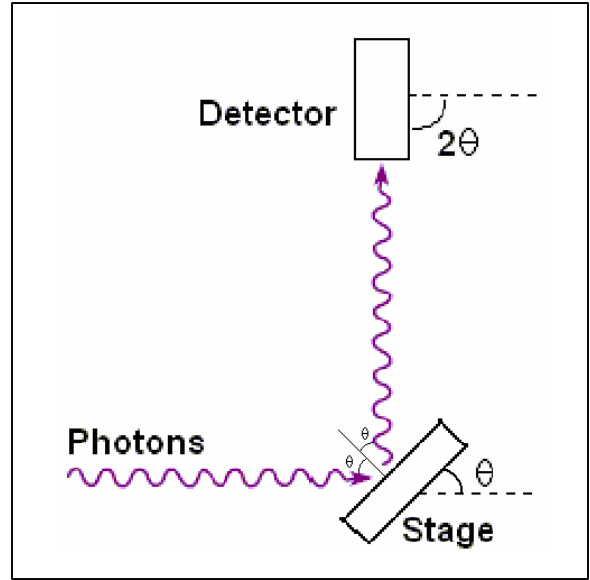


Figure 3.3: Reflectometer schematic. [15]

The first step in data collection is determining the dark current offset. The beam is blocked by a glass filter and the current in the photodiode is measured. This offset is subtracted from every subsequent photodiode reading. It appears to be angle dependent, which is factored into later calculations. An  $I_0$  reading is then taken. The stage is dropped down and the detector is zeroed so that the beam is pointing directly into it. This measurement serves as a normalization reference. The actual reflection measurement is then performed. Both these readings are linearly normalized to the beam current. The final reflectance is calculated using normalization programs found on the computers at the beamline. The two programs used were “normalize” and “normscript.” They are based off the following equation:

$$R = \frac{I_r - I_d}{I_0 - I_d} \cdot \frac{B_0}{B_r} \quad (3.1)$$

- $I_r$  = photodiode current of run
- $I_0$  = photodiode current of normalization run
- $I_d$  = photodiode current of dark current offset
- $B_0$  = beam current at time of  $I_0$  run
- $B_r$  = beam current at time of  $I_r$  run

Transmission is calculated in a similar manner. The Moxtek transmission window is mounted on the stage and is rotated to 90 degrees, so as to be perpendicular with the incoming beam. The stage can then be rocked to obtain transmission at other angles close to normal. Separate transmission measurements of both the window and the window coated with the thorium film must be taken to factor out the effect of the window.

Transmission is calculated for these two runs using equation 3.1. The transmission of the window with the thorium film is then divided by that of just the window to obtain the true transmission of just the thorium film. This method does not take into account the reflectance of the thorium film and the window. This is a problem, especially when the incident angle deviates significantly from normal. The high absorption of the polymer film also adds a degree of uncertainty into this technique.

$\beta$  is calculated experimentally at the ALS using the following equation [9]:

$$I = I_0 e^{-az} \quad (3.2)$$

- $I$  = transmitted intensity
- $I_0$  = initial intensity
- $z$  = film thickness
- $a$  = linear absorption coefficient

The linear absorption coefficient,  $a$ , is given by:

$$a = \frac{4pb}{\lambda} \quad (3.3)$$

- $\lambda$  = wavelength in vacuum

### 3.2 Reflectance Data

Figure 3.4 shows the reflectance of Th001 as a function of wavelength at incident angles of 5, 10, and 15 degrees from grazing. As expected, reflectance decreases as the angle from grazing increases. At angles closer to grazing, the light interacts through a longer distance with the highly reflective thorium atoms. Its path also doesn't need to be diverted as severely. The structure of the curve is essentially consistent among the three angles. Between about 12 to 16 nm, there is a sharp dip in reflectance, including smaller secondary peaks. A small absorption at about 4.5 nm on the 5 degree curve is also noticeable. This is attributed to the presence of airborne carbon contaminants which have accumulated on the surface.

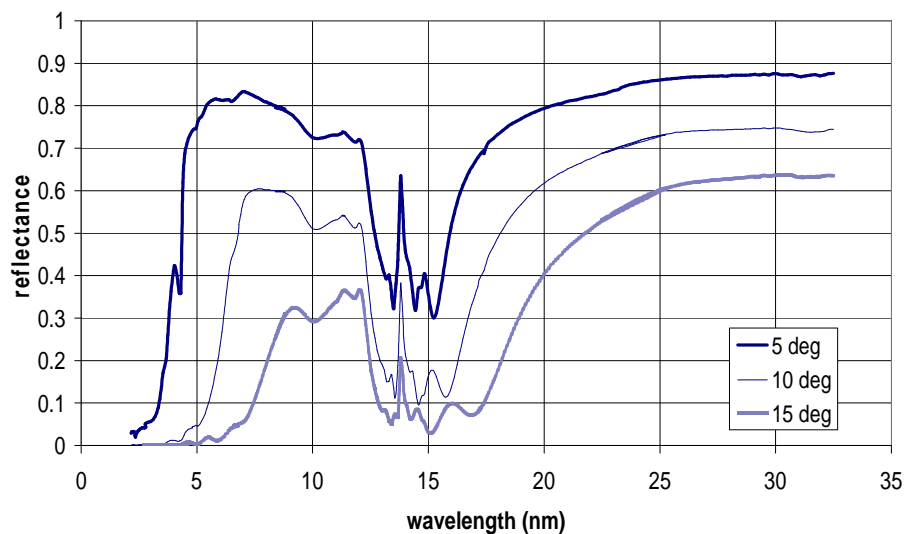
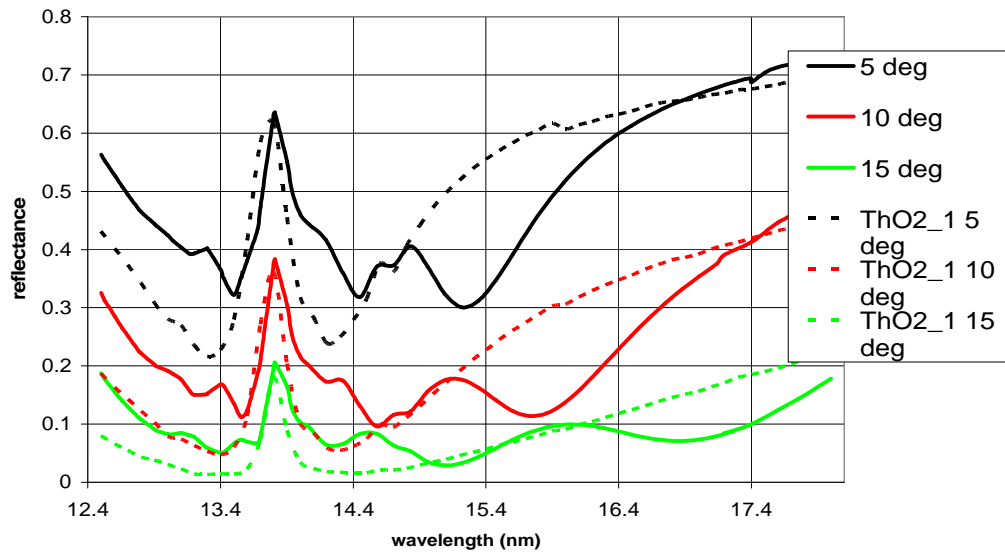


Figure 3.4: Reflectance of Th001 vs. wavelength at 5, 10, and 15 deg from 2 to 32 nm.

The reactively sputtered ThO<sub>2</sub>\_1 (44.1 nm) sample was also analyzed at ALS and its reflectance was compared to Th001. Only the region exhibiting a high amount of structure from 12.5 to 18.0 nm has been looked at to date. This comparison is shown graphically in figure 3.5.



**Figure 3.5: Reflectance of Th001 and ThO<sub>2</sub>\_1 vs. wavelength at 5, 10, and 15 deg. from 12.5 to 18.0 nm. Th metal is shown using solid lines and thorium dioxide is dashed.**

Figure 3.5 demonstrates that the reflectance of thorium metal is generally higher than its oxide. This is an area of low reflectance in the thorium reflection spectrum because of absorption edges. Most of the structural features in this range are due to the presence of thorium and not oxygen. In certain regions, the increase in oxygen content actually diminishes the effect of certain absorption energies and makes ThO<sub>2</sub> the better reflector. The discrepancy in curve shape between different angles could possibly be attributed to thin film interference effects.

Iridium, gold, and nickel are commonly used EUV reflectors. A previous study was performed by the group which compared these materials to uranium nitride and uranium oxide. [33] Figure 3.6 shows the reflectance spectra of Th001 plotted against UN, NiO/Ni, Au, and Ir.

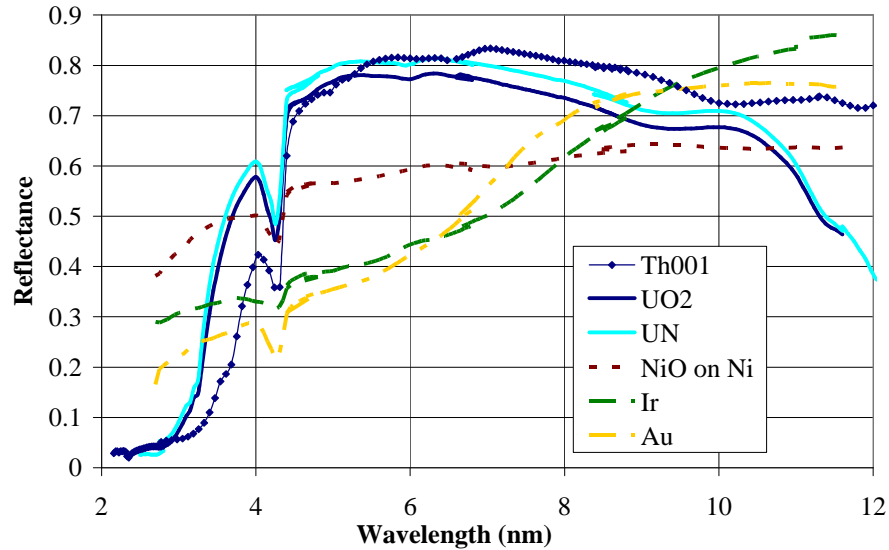


**Figure 3.6: Measured reflectance of Th001, UO<sub>2</sub>, UN, NiO on Ni, Ir, and Au vs. wavelength at 5 degrees from 2 to 12 nm. Th reflects highest from 6.5 to 9.4 nm.**

A feature at 4.5 nm is common to all the spectra and is thought to be due to the carbon edge. From about 6.5 to 9.4 nm, thorium exhibits higher reflectance than any material tested thus far. This encouraging result validates predictions based on CXRO. This will be addressed in further detail in the next section.

### 3.3 Transmission Data

The Th003 deposition created both a reflection and transmission sample. Figure 3.7 shows the curves from these data plotted together. Prominent features, such as the

spikes seen at close to 13.8 nm in both, show the compatibility of the absorption and reflection spectra.

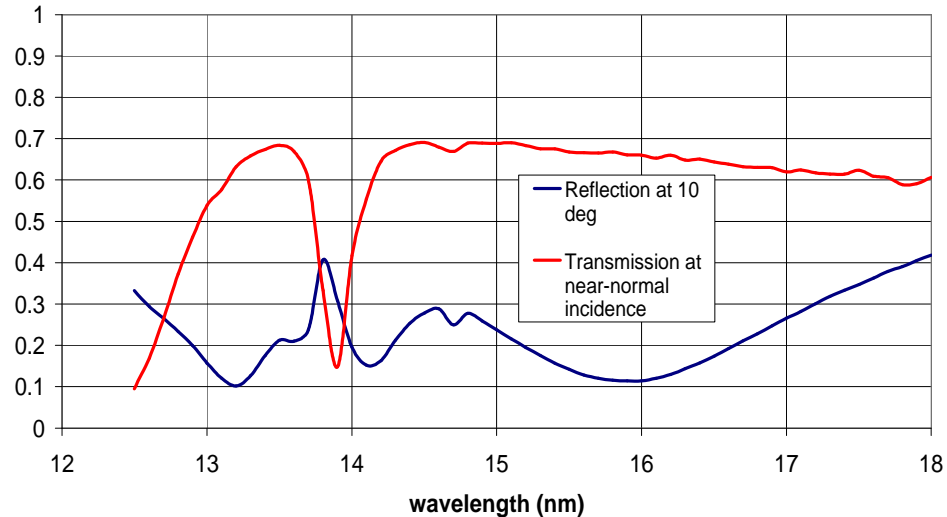


**Figure 3.7: Reflection and transmission of Th003.**

Transmission data was taken in half degree increments at incident angles of up to 30 degrees from normal. There was a slight variance in the amplitude of the transmission as a function of angle. The shape of the graph was otherwise preserved. The data at normal incidence, however, is a strange anomaly. Its shape was consistent, but was offset inexplicably from the other angles. This was true at both wavelengths we measured. Even the data at only 0.5 degrees away was grouped with the rest. No satisfactory explanation has been determined for this phenomenon, and it will be researched further at upcoming ALS trips.

The absorption coefficient,  $\beta$ , of the complex index of refraction was calculated as a function of wavelength from the Th003 transmission data using equations 3.2 and 3.3. Visible in figure 3.8 is the absorption peak referred to in the previous paragraph. There is also a dramatic increase in beta as the wavelength decreases below 13 nm.

XANES measurements taken from both a naturally oxidized thorium film (Th004) and a reactively sputtered ThO<sub>2</sub> film (ThO2\_1) are also included. The y-axis label “beta” does not apply to the XANES curves; unitless, relative intensity is represented instead.

Common features show a correlation between the measurements, while differences, such as the small peak at 14.1 nm in ThO<sub>2</sub>, indicate that there could be differences in the optical constants of Th and ThO<sub>2</sub>. Other regions of the EUV also merit further analysis.

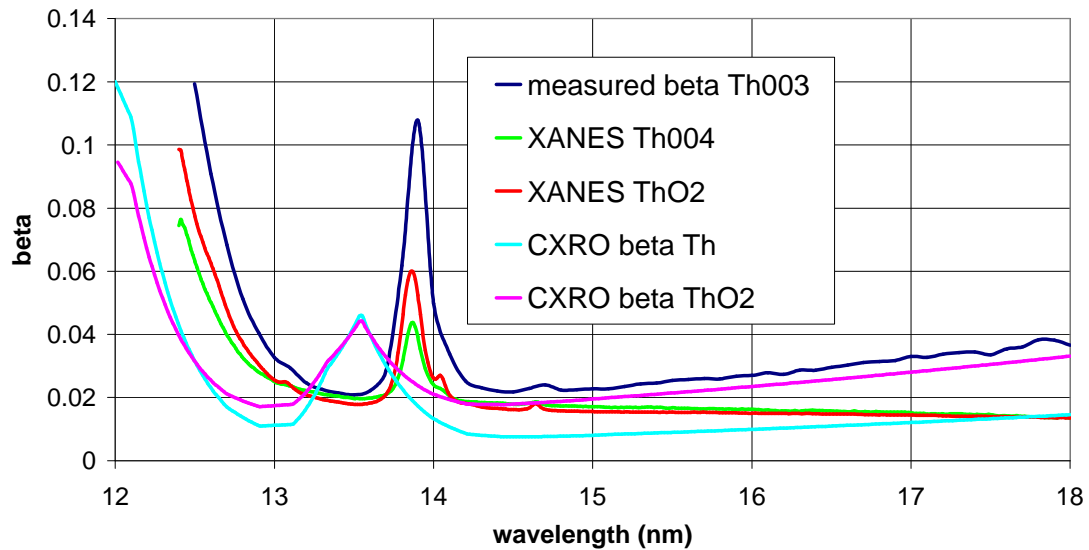


**Figure 3.8: Measured absorption coefficient  $\beta$  vs. CXRO data as a function of wavelength. XANES measurements are compared to  $\beta$ .**

### 3.4 Comparison to Theory

Although our model correctly accounts for some of the features of the measured data, there are a number of inconsistencies which deserve further investigation. Figure 3.9 shows the 10 degree measured spectra from figure 3.4 plotted alongside the corresponding CXRO/IMD curve.

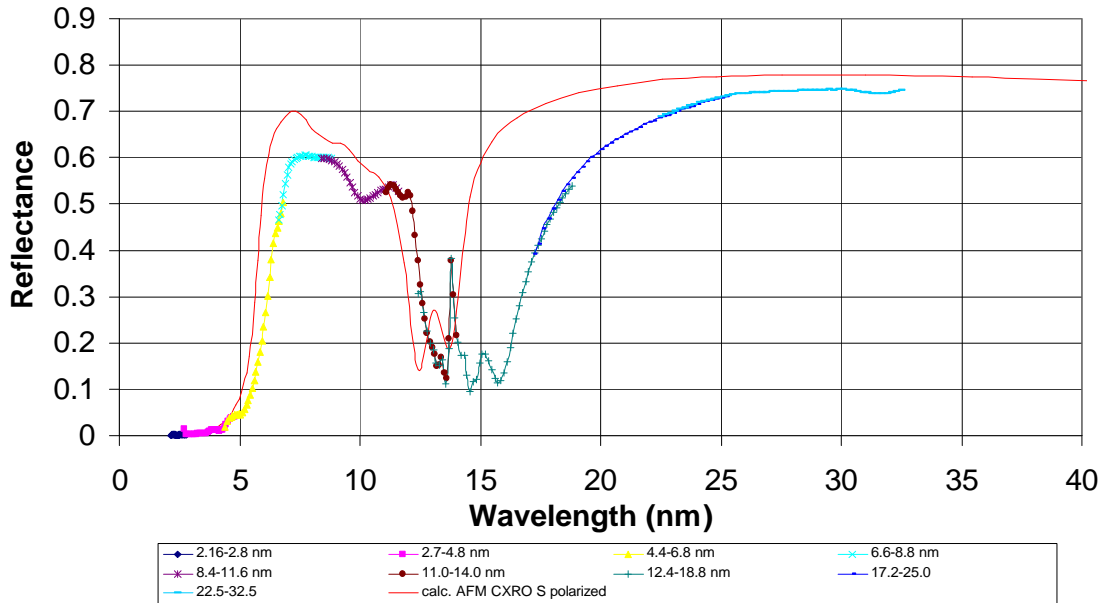


**Figure 3.9: Measured (Th001) and computed reflectance of thorium at 10 deg. from 2 to 32 nm. The red curve is computed from CXRO data.**

The continuity of the measured curve was a major group success. In past trips to the ALS, data taken from different filters did not overlap well. This added uncertainty to the data and lowered the presentation quality. I attribute a more systematic and organized approach to taking data as the solution to this problem. All three angles (5, 10, 15) overlapped almost flawlessly.

While the overall shapes of the measured and calculated spectra are remarkably consistent, the plots do not line up. There is a shift in energy (x-axis) of up to 20 eV in certain areas of the spectrum. As a consequence of this, specific energies with predicted reflectances in the neighborhood of 70% are as low as 10% (~78 eV). This large discrepancy is an interesting scientific problem.

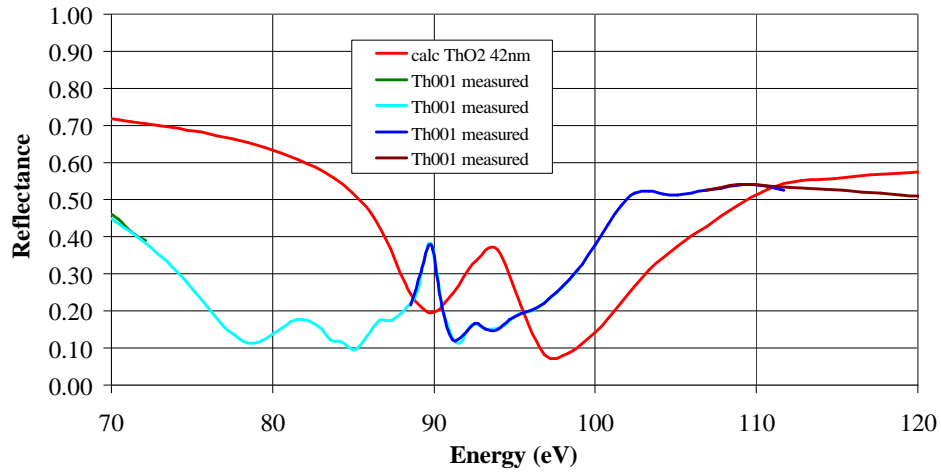


**Figure 3.10: Measured (Th001) and computed reflectance of thorium at 10 deg. from 70 to 120 eV.**

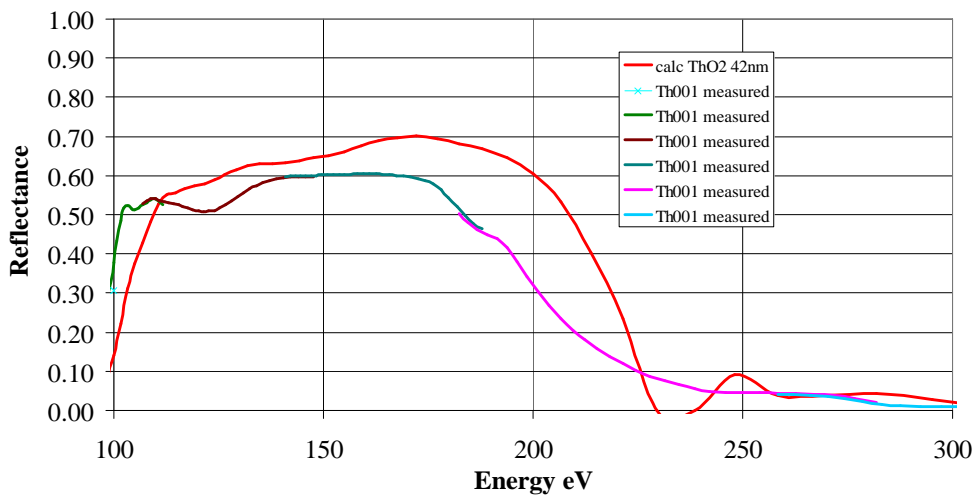


**Figure 3.11: Measured (Th001) and computed reflectance of thorium at 10 deg. from 100 to 300 eV.**

Chemical bonding is important in determining optical properties at visible wavelengths. An example of this is quartz. This silicon dioxide crystal is transparent at optical wavelengths even though it consists of silicon, which is opaque in its elemental form. Somehow, the bonding between the oxygen and silicon atoms in the lattice allows light to be transmitted. The conventional method of combining atomic scattering factors

disregards this phenomenon on the basis that it will not have an effect on higher energy radiation. [9] It is unclear where in the electromagnetic spectrum neglecting bonding becomes a valid assumption. With observed deviations as high as 20 eV, we have confirmed the observations of others that chemical bonding is significant in the EUV.

This explanation alone does not account for the dramatic energy shifts we observe. The reasonable conclusion is that the CXRO data is incorrect in certain energy ranges. Our data has been measured carefully, using different methods and more modern, capable equipment.

Henke and his colleagues obtained the atomic scattering factors used on CXRO for all the elements from hydrogen to uranium, for photon energies extending from the extreme ultraviolet up to hard x rays. They first determined  $f_2$  by measuring the transmission through known amounts of the element. In the case of metals, thin sheets were used. If  $f_2$  is known across a sufficiently broad range of frequencies,  $f_1$  can be inferred by the Kramers-Kronig relation, which is given by [9]:

$$f_1(\omega) - Z = -\frac{2}{\pi} P_C \int_0^{\infty} \frac{u \cdot f_2(u)}{u^2 - \omega^2} du \quad (3.4)$$

- $\omega$  = angular frequency
- $Z$  = atomic number

From  $f_1$  and  $f_2$ , the optical constants  $d$  and  $\beta$  can easily be calculated as seen in equations 1.18 and 1.19. Thus, experimental determination of both  $d$  and  $\beta$  can depend only on one transmission measurement. There are errors which could have affected this measurement, such as beam reflection or imprecise characterization of the material. The data from this technique clearly don't work well in predicting the reflectance of our samples. For this reason, we trust the constants we extract from our data to be more accurate.

This project does not offer an explanation of the optical property differences between thorium and its oxide. This is certain to be an interesting and challenging theoretical project which could possibly involve band structure and bonding analysis.

Achieving a better understanding of the interaction between EUV radiation and thorium compounds requires better characterization of our mirrors. The rate and manner of oxidation in thorium thin films undeniably has a large effect on the optical properties of the metal. Presently, additional research is being performed in this area.

## CHAPTER IV. OPTICAL CONSTANT FITTING

### 4.1 Fitting Overview

The JFit program [34], written by Dr. R. Steven Turley and Niki Farnsworth, can be used to fit optical constants from transmission data. The program is currently being modified to include both transmission and reflectance data. It iterates through thickness and the optical constants  $n$  and  $k$ , using a least squares procedure to find the most accurate fit. The EUV transmission of Th003 was measured at the ALS at different sample angles and read into the program. Its fit was based off the following equations [25]:

$$P_{tot} = Ae^{-c^2} \quad (4.1)$$

$$c^2 = \sum_i \frac{\{x_i - x'_i(n, k, z)\}^2}{2s_i^2} \quad (4.2)$$

- $P$  = probability function
- $A$  = scaling amplitude
- $x$  = data point
- $x'$  = fit point (function of  $n$ ,  $k$ , thickness)
- $s$  = uncertainty in data (standard deviation)

If the fit and the data are in close agreement over the entire range of angles, the  $c^2$  function will be small. This corresponds to a high value of  $P$ . The program runs within the constraints it has been given by the user until it finds the highest  $P$ . First, the Moxtek transmission window data was fit. This determines its optical constants and thickness, which lowers the number of parameters in the thorium fit.

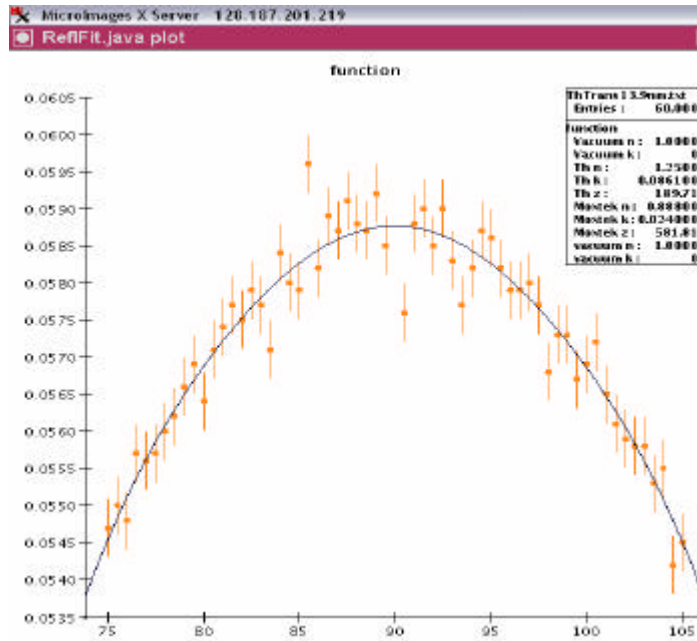


Figure 4.1: Transmission data and fit as a function of angle at 13.9 nm. [25].

## 4.2 Results and Comparison

The constants from only two wavelengths, 13.9 and 17.0 nm, have been fit to date. 13.9 nm was selected because it should be near the top of an absorption peak. Figure 4.1 shows the data and fit at this wavelength. We assigned a small offset of one degree to the incident angle of the film, which produced better fits. This can be explained physically because the film has been compressed and crinkled by thin film deposition. The fit appears to be very good, especially given the noisy data. The 17.0 nm data was similar. The constants derived from these wavelengths are shown below in table 4.1.

	13.9 nm	17.0 nm
Th n	1.2500 +/- 0.3056	1.3076 +/- 0.0298
Th k	0.0861 +/- 0.0072	0.0267 +/- 0.0007
Th z (nm)	18.972 +/- 0.548	19.797 +/- 0.461
Moxtek n	0.888	0.6492
Moxtek k	0.024	0.032
Moxtek z (nm)	58.182 +/- 1.116	58.129 +/- 0.277
$\chi^2$	1.00137	0.98217

**Table 4.1: Optical constants obtained from transmission data fits at 13.9 and 17.0 nm. [25]**

The  $\chi^2$  function has been modified from its explanation in section 4.1 to scale the error. A value close to one is desirable. The thicknesses (Th z) obtained from the fit agree well with the measured XRD value of 19.7 nm. (table 2.1) All the uncertainties are also very low, with the exception of the index of refraction (Th n) at 13.9 nm. Nevertheless, it is reasonable enough to preserve the validity of the other fit parameters. The data from these fits were compared to the values obtained from the alternative method reported in section 3.3.

Wavelength (nm)	Beta Calculated	Beta Fit	Percent Disagreement
13.9	.1078	.0861	20.1
17.0	.0330	.0267	19.1

**Table 4.2: Comparison of two methods of beta determination.**

The agreement is fairly good between these two methods of determining beta. The percent difference is close to twenty in both. Additional fits at different wavelengths are needed to construct a curve to compare against figure 3.8.

## CHAPTER V. CONCLUSIONS

Thorium was found to be a viable alternative to conventionally used reflectors in the EUV. Between 6.5 and 9.4 nm, it reflected better at 5 degrees than uranium oxide, uranium nitride, gold, iridium, and nickel. Analysis over additional energy ranges could yield more encouraging results. Such a material could enhance present technology as well as pioneer new ones.

Concerns such as film oxidation complicate characterization and alter reflectance. The reflectance of  $\text{ThO}_2$  was generally confirmed to be less than that of oxidized thorium metal from 12.5 to 18.0 nm. Increasing oxidation observed in successive XRD runs was not quantitatively reported. The rate did appear to be noticeably less than uranium's. XPS indicated a decreasing concentration of  $\text{ThO}_2$  as film depth increased. The width of the peak indicates that the dioxide is mixed with the metallic thorium, rather than existing as an intermediate  $\text{ThO}$  oxidation state.

The general agreement between the two methods of beta determination was encouraging. This indicates the probable validity of the corresponding delta values from the fit. When the JFit program is able to process both absorption and reflection data, we will have a better idea of the actual values. Oxide layers will also need to be taken into consideration.

XANES measurements suggest that  $\text{ThO}_2$  behaves differently in the EUV than Th. Consequently, atomic scattering factors cannot be directly applied to compounds. A possible modification is the introduction of molecular scattering factors. This could be an extensive theoretical project.

There was a large discrepancy between the measured and calculated thorium reflectance curves. Possible explanations such as film contamination and systematic error have been discounted because of data reproducibility and the sheer size of the inconsistency. It is more likely that the atomic scattering factors on CXRO are not correct and need to be updated with newer data.

## REFERENCES

- [1] <http://www.research.ibm.com/journal/rd/411/chiu.html>, June 5, 2004.
- [2] K. Takemoto, et. al., "Transmission x-ray microscopy with 50 nm resolution in Ritsumeikan synchrotron radiation center," X-ray Microscopy AIP conference proceedings 446-51 (2-6 Aug 1999).
- [3] D. D. Allred, M. B. Squires, R. S. Turley, W. Cash, and A. Shipley. "Highly reflective uranium mirrors for astrophysics applications," Proc. SPIE **4782**, 212-223 (2002).
- [4] S. Lunt, "Determining the indices of refraction of reactively sputtered uranium dioxide thin films from 46 to 584 angstroms," M.S. Thesis (Brigham Young University, Provo, UT, 2000).
- [5] D. J. Griffiths, *Introduction to Electrodynamics*. Prentice Hall, Upper Saddle River, New Jersey, 1999, p. 383.
- [6] V.G. Kohn. "On the theory of reflectivity by an x-ray multilayer mirror," Phys. Stat. Sol. **185**(61), 61-70 (1995).
- [7] L.G. Parratt. "Surface studies of solids by total reflection of x-rays," Physical Review **95** (2), 359-369 (1954).
- [8] E. Spiller, *Soft X-ray Optics*, (SPIE Optical Engineering Press, 1994), p.6-13.
- [9] D. Attwood. *Soft X-Rays and Extreme Ultraviolet Radiation*. Cambridge University Press, Cambridge, 1999.
- [10] <http://www.campusprogram.com/reference/en/wikipedia/t/th/thorium.html>, June 5, 2004.
- [11] [http://www.ccnr.org/decay\\_U238.html](http://www.ccnr.org/decay_U238.html), June 5, 2004.
- [12] <http://www.webelements.com/webelements/elements/text/U/phys.html>, June 5, 2004.
- [13] <http://environmentalchemistry.com/yogi/periodic/Th.html>, June 7, 2004.
- [14] <http://www.processmaterials.com/oxides.html>, June 7, 2004.

- [15] M. Urry. "Determining Optical Constants of Uranium Nitride Thin Films in the Extreme Ultraviolet (1.6-35 nm)," Undergraduate Thesis (Brigham Young University, Provo, UT, 2004).
- [16] [http://www-cxro.lbl.gov/optical\\_constants/mirror2.html](http://www-cxro.lbl.gov/optical_constants/mirror2.html), January 22, 2004.
- [17] D. Windt, "IMD—software for modeling the optical properties of multiplayer films," *American Institute of Physics* **12** (4), 360-370 (1998).
- [18] R.M. Dell, V.J. Wheeler, and N.J. Bridger. "Hydrolysis of uranium mononitride," *Faraday Soc. Trans.* **63**, 1286-94 (1967).
- [19] <http://www.uksaf.org/tech/edx.html>, May 20, 2004.
- [20] <http://volta.byu.edu/adamson03.pdf>, November 11, 2003.
- [21] Bomben, Kenneth D., John F. Moulder, Peter E. Sobol, and William F. Stickle. *Handbook of X-Ray Photoelectron Spectroscopy*. Eden Prairie, Minnesota: Physical Electronics, Inc., 1995.
- [22] Kristi Adamson (data provided by)
- [23] <http://www.uksaf.org/tech/nexafs.html>, May 20, 2004.
- [24] <http://www.weizmann.ac.il/surflab/peter/afmworks/>, November 4, 2003.
- [25] N. Farnsworth. "Roughness and other fun stuff." XUV Group Powerpoint Presentation (Brigham Young University, Provo, UT, 2004)
- [26] P. Debye. *Über die Intensitätsverteilung in den mit Röntgenstrahlung erzeugten Interferenzbildern.* *Verh. D. Deutsch. Phys. Ges.* 15: 738.
- [27] P. Croce and L. Nevot. *Étude des couches minces et des surfaces par réflexion rasante, spéculaire ou diffuse, de rayons X.* *De Physique Appliquée* 11 (1976): 113-125.
- [28] Winston Larson (data provided by)
- [29] <http://www1.physik.tumuenchen.de/~gammel/matpack/html/Nuclear/Elements/lattice.html>, July 1, 2004.
- [30] <http://www-als.lbl.gov/als/aboutals/alsquickfacts.html>, June 5, 2004.
- [31] [http://www-als.lbl.gov/als/als\\_users\\_bl/6.3.2-Datasheet.pdf](http://www-als.lbl.gov/als/als_users_bl/6.3.2-Datasheet.pdf), August 5, 2003.
- [32] <http://www.lbl.gov/>, September 8, 2003.

[33] R. L. Sandberg, D. D. Allred, J. E. Johnson, R. S. Turley, “A comparison of uranium oxide and nickel as single-layer reflectors from 2.7 to 11.6 nm,” in *Advances in Mirror Technology for X-Ray, EUV Lithography, Laser, and Other Applications*, edited by Ali M. Khounsary, Udo Dinger, Kamuya Ota, Proceedings of SPIE Vol. 5193 (SPIE, Bellingham, WA, 2004) 191-203.

[34] R.S. Turley, *fitals.f*, Brigham Young University, 2003.